Article

Ideal Strength and Deformation Mechanism in High-Efficiency Thermoelectric SnSe

Guodong Li, Umut Aydemir, Max Wood, William A. Goddard, Pengcheng Zhai, Qingjie Zhang, and G. Jeffrey Snyder

Chem. Mater., **Just Accepted Manuscript** • DOI: 10.1021/acs.chemmater.7b00279 • Publication Date (Web): 21 Feb 2017

Ideal Strength and Deformation Mechanism in High-Efficiency Thermoelectric SnSe

Guodong Li [†,‡], Umut Aydemir [‡], Max Wood [‡], William A. Goddard III [⊥], Pengcheng Zhai [†], Qingjie Zhang [*,†], and G. Jeffrey Snyder [*,‡]

[†]State Key Laboratory of Advanced Technology for Materials Synthesis and Processing, Wuhan University of Technology, Wuhan 430070, China.

[‡]Department of Materials Science & Engineering, Northwestern University, Evanston, Illinois 60208, USA.

[⊥]Materials and Process Simulation Center, California Institute of Technology, Pasadena, California 91125, USA.

[*]Corresponding authors: jeff.snyder@northwestern.edu; zhangqj@whut.edu.cn

Abstract: The widespread use of thermoelectric conversion technology requires thermoelectric materials of high thermoelectric efficiency and high fracture strength. Single crystal SnSe shows an extremely high *zT* value in the moderate temperature range, but its mechanical properties have rarely been studied so far. Here we use density functional theory to determine the ideal strength and deformation mechanism of perfect SnSe single crystals for shear deformations. The lowest ideal strength of SnSe is found to be 0.59 GPa under the (100)/<001> shear load, which agrees with experimental evidence that single crystals cleave along the (100) slip plane. The van der Waals-like Se−Sn bond, which couples the different Se-Sn layered substructures, is much softer than the covalent Se−Sn bond which constructs the Se-Sn layered substructure. This creates pathways of easy slip between Se-Sn layered substructures, which can release shear stress and lead to structural failure. Meanwhile, the layered substructures themselves can resist shearing within the (100)/<001> slip system. These results provide a plausible atomic explanation to understand the intrinsic mechanics of SnSe.

1. INTRODUCTION

Thermoelectric (TE) technology, which can enable the direct conversion of heat into electricity with high reliability and no moving parts, plays an important role in the exploration of sustainable clean energies.[1] The conversion efficiency of TE materials or devices is determined by the dimensionless figure of merit (*zT*), which is defined as $zT = \alpha^2\sigma T/\kappa$, where α is Seebeck coefficient, σ is electrical conductivity and κ is thermal conductivity.[2] In the past two decades,

the TE field has developed several strategies to improve a material's *zT*, such as phonon glass electron crystal (PGEC),[3,4] band engineering,[5,6] nanostructuring, [7-9] and large lattice anharmonicity.[10,11] Widespread applications of this promising technology necessitates both *n*- and *p*-type that are mechanically compatible and retain their desired electrical and mechanical properties of TE devices upon cycling.[12]

SnSe, a simple layered crystal consisting of earth abundant elements, recently attracted much attention surprising the scientific community with the high *zT* of 2.6 along the *b* axis in the orthorhombic unit cell and a *zT* of 2.3 along the *c* axis.[13-18] SnSe behaves as a *p*-type material with a large energy gap of 0.86 eV,[19] which makes doping SnSe with donor or acceptor atoms not as straightforward as in the case of PbTe and PbSe. However, sodium has been found to be an effective acceptor dopant which can increase the *zT* from 0.1 to 0.7 at 300 K along the *b* axis while obtaining a maximum *zT* of 2.0 at 773 K.[20] Thus, a device *ZT*, which determines the overall TE conversion efficiency of a device, of 1.34 from 300 to 773 K is obtained, leading to a theoretical conversion efficiency of 16.7% at T_c = 300 K and T_h = 773 K in hole-doped SnSe. This efficiency is much higher than that of other high performance TE materials such as PbTe.[21] However, for engineering applications of SnSe, one critical challenge is to mitigate the thermo-mechanical stresses arising from temperature gradients,[22] which requires SnSe to have robust mechanical properties. However, the intrinsic mechanical properties and the mechanism for brittle failure of SnSe remain unknown until now.

In order to understand the intrinsic mechanics and determine the deformation mechanism in layered SnSe, we apply density functional theory (DFT) to investigate the shear deformation properties of single-crystal SnSe. We find that shearing along the (100)/<001> slip system has the lowest ideal strength of 0.59 GPa, suggesting that it is the most plausible slip system to lead to failure. This analysis is bolstered with experimental evidence that shows slip usually occurs on the (100) plane between the layered substructures. Because the van der Waals-like Se–Sn bond is much softer than the covalent Se–Sn bond, shear deformation leads to slip between the Se-Sn layered substructures while the layered substructures themselves can stably hold together. The (001)/<010> slip system has a higher ideal strength of 2.81 GPa compared with (100)/<001> and (100)/<010> slip system because the covalent Se–Sn bond is much stronger than the van der Waals-like Se–Sn bond in resisting shear deformation. The failure along this system arises from the breakage of the covalent Se–Sn bond. Here we suggest improving the van der Waals-like Se–Sn coupling interactions between layered substructures to prevent or postpone slip to enhance the ideal strength by proper doping strategies, *e.g.,* the partial substitution of Sn by Ge or Se by S.

These results based on a plausible atomic explanation in understanding of the intrinsic mechanics of SnSe could be applied to other important TE and non-TE related energy materials research.

For single crystalline SnSe, very low thermal conductivity was reported along with record-high zT of 2.6 along the b-axis.[13] However no other group can verify this result so far, which was recently addressed.[23,24] Even in polycrystalline SnSe, the highest zT value of doped SnSe was ~1.0.[25-29] Possible reasons for the unreproducible thermal conductivity data were discussed in both in detail and were related to surface oxidation, low density, large number of intrinsic defects, etc.[23,24] Based on our results, the lowest ideal strength was found along the (100) plane, which could lead to formation of cracks and hence lower the density, which may partially account for the (controversial) ultralow thermal conductivity of SnSe crystals.[23,24]

2. METHODOLOGY

All DFT calculations were performed with the Vienna ab initio Simulation Package (VASP), using the Perdew-Burke-Ernzerhof (PBE) exchange-correlation functional and the projector augmented wave (PAW) method to account for the core-valence interactions.[30-32] A plane wave cutoff energy of 500 eV and a 4×10×10 Monkhorst-Pack uniform k-point reciprocal space sampling were adopted since they give excellent convergence of the total energies and structural parameters. The convergence criteria were set to 1×10^{-6} eV energy difference for solving the electronic wave function and 1×10^{-2} eV/Å force for geometry optimization. The optimized SnSe orthorhombic unit cell (*Pnma* (62) space group) parameter is a = 11.774 Å, b = 4.216 Å, c = 4.527 Å, which is only 2.37%, 1.52%, and 1.84% larger than the experimental value of a = 11.501(2) Å, b = 4.153(1) Å, c = 4.445(1) Å.[33] Our optimized lattice parameter is very close to previous *ab initio* calculation of a = 11.790 Å, b = 4.219 Å, c = 4.524 Å using PBE.[34]

The quasi-static shear loading of SnSe is achieved by imposing the uniaxial shear deformation on a specific direction while allowing full structural relaxation of the atoms for the other five strain components. The residual stresses for relaxation of these five strain directions are all less than 0.1 GPa. The detailed simulation setup is the same with our previous study.[35] This relaxation method has been proven to be an effective tool to shed lights on the intrinsic failure mechanism at the atomic scale.[36,37] For the shear deformation of SnSe, (100)/<010>, (100)/<001>, and (001)/<010> slip systems were considered with all the supercells containing 128 atoms.

3. RESULTS AND DISCUSSION

3.1 Crystal structure of SnSe

SnSe has a simple layered orthorhombic structure crystallizing in the *Pnma* (62) space group at room temperature.[13] Figure 1 shows views of the SnSe structure along *a*, *b*, and *c* axes. The crystal structure contains 8 atoms in the unit cell, which form a layered substructure along the *b*-*c* plane. Se and Sn atoms, linked with strong covalent Se–Sn bonding (~2.80 Å) within the substructure, create zig-zag chains along the *b* axis, while the layered substructures in the unit cell are coupled by a weak van der Waals-like Se–Sn interaction (~3.50 Å) along the *a*-axis.

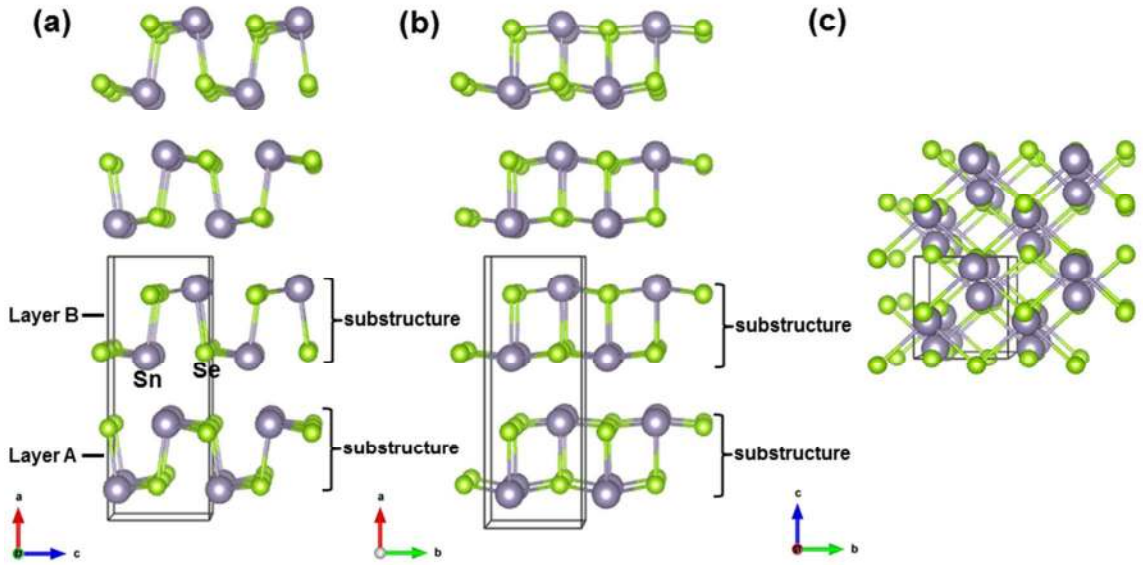

Figure 1. Crystal structure of the room temperature phase (*Pnma*) for SnSe. Structure along the *b* axis (a), the *c* axis (b), and the *a* axis (c). The black solid line represents an orthorhombic unit cell containing 8 atoms. The Sn and Se atoms are represented with gray and green balls, respectively. In the unit cell, the covalent Se–Sn bonds construct the Se-Sn layered substructure, and the van der Waals-like Se–Sn interactions couple the layered substructure A and B, as shown in Figure1 (a).

3.2 Elastic properties of SnSe

The elastic properties were calculated to validate our methodology and provide valuable information on the stiffness of SnSe. The elastic constants (C_{11}, C_{12}, C_{13}, C_{22}, C_{23}, C_{33}, C_{44}, C_{55}, C_{66}) were obtained by calculating the total free energy as a function of various small lattice

distortions δ from the optimized unit cell. Based on the calculated elastic constants, the related elastic properties such as the bulk modulus (B), shear modulus (G), Young's modulus (E), Poisson's ratio (v), and ductility index (B/G) can be computed using the Voigt-Reuss-Hill method.[38] Table 1 lists the calculated elastic mechanical properties (C_{11}, C_{12}, C_{13}, C_{22}, C_{23}, C_{33}, C_{44}, C_{55}, C_{66}, B, G, E, v, B/G), which agrees with previous reported *ab-initio* calculation using the PBE functional.[39]

A simple relationship, B/G, can empirically estimate the ductility and brittleness of a material. A high B/G ratio corresponds to the ductile nature, while a low ratio is associated with the brittleness. The critical value suggested by Pugh is B/G = 1.75.[40] Here, the calculated B/G value of SnSe is 1.41, indicating this material is brittle.

Table 1. Calculated elastic constants (C_{11}, C_{12}, C_{13}, C_{22}, C_{23}, C_{33}, C_{44}, C_{55}, C_{66}) and other related elastic properties: bulk modulus (B), shear modulus (G), Young's modulus (E), Poisson's ratio (v) and ductility index (B/G) of SnSe, and previous *ab-inito* results. The unit of elastic constants and various modulus is GPa.

Method	C_{11}	C_{12}	C_{13}	C_{22}	C_{23}	C_{33}	C_{44}	C_{55}	C_{66}	B	G	E	v	B/G
Our PBE	41.1	7.33	12.1	65.7	26.9	29.6	12.0	29.6	14.7	24.1	17.1	41.4	0.21	1.41
PBE[33]	39.3	8.1	12.9	66.7	27.5	29.8	11.9	28.4	14.4	24.4	14.7	-	0.25	-

3.3 Ideal shear strength of SnSe

Figure 2 shows the shear stress-strain relationships of SnSe at 0 K along various slip systems. All the shear stresses linearly increase with the shear strain at the initial loading stage. The (100)/<010> and (100)/<001> systems show a similar moduli, which is lower than that of the (001)/<010> system. This suggests that the (100)/<010> and (100)/<001> systems are much weaker than the (001)/<010> system in resisting the external deformation. Then the shear stress gradually increases until reaching the ideal strength in both the (100)/<010> and (100)/<001> systems. However, in the (001)/<010> system, the shear stress suddenly drops to 0.76 GPa at 0.07 strain, and then sharply increases to the point of maximum stress, indicating a significant structural rearrangement at 0.07 strain. Beyond the maximum stress, the decreased shear stress shown in Figure 2 represents the softening stage of SnSe before the failure. Finally, the shear stress suddenly drops to zero. This indicates that the system can no longer resist the external deformation, leading to structural failure. Shearing along the (100)/<001> system has the lowest

shear strength of 0.59 GPa, suggesting it is the most likely plausible slip surface under pressure. The maximum shear strength (0.78 GPa) along the (100)/<010> slip system is slightly higher than the (001)/<010> system. The van der Waals-like Se−Sn bonds along the *a*-axis has a much larger stretching ratio than the covalent Se−Sn bond as shown in Figure 3(d) and 4(d). For example, the van der Waals-like Se−Sn3 bond has a stretching ratio of 5.65% and the covalent Se−Sn1 bond has a much lower stretching ratio of 1.42% as shown in Figure 4(d). This suggests the van der Waals-like Se−Sn bond dominates the structural deformation, indicating the van der Waals-like Se−Sn bond is responsible for the maximum shear strength along the (100)/<010> and (100)/<001> systems. Thus, (100)/<010> and (100)/<001> slip systems show a lower maximum shear strength of 0.59 and 0.78 GPa, respectively. However, the maximum shear strength (2.81 GPa) along the (001)/<010> slip system is much higher compared with (100)/<001> and (100)/<010> systems, because the covalent Se−Sn bond has a much larger stretching ratio, *ie.,* 18.87% for covalent Se1−Sn1 bond as shown in Figure 5(d), indicating the covalent Se−Sn bond is responsible for the maximum shear strength along this slip system. The ideal shear strength (0.59 GPa) of SnSe is much lower than the ideal shear strength of other high-performance thermoelectric materials such as $CoSb_3$ (7.17 GPa) [35] and TiNiSn (10.52 GPa),[41] which demonstrates that SnSe has a significantly lower ideal strength.

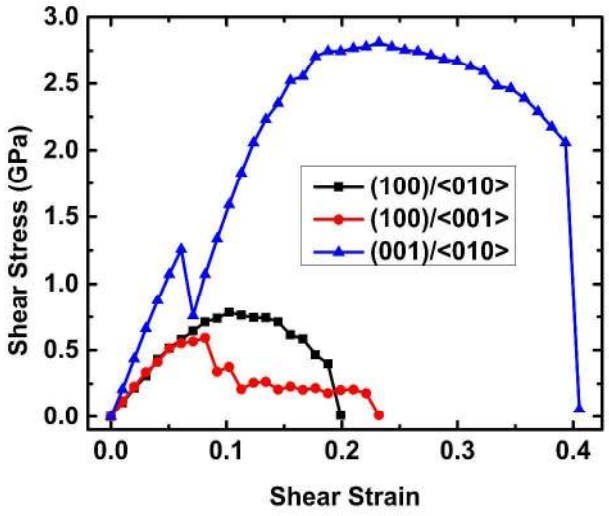

Figure 2. Calculated shear stress vs. strain of SnSe under different shear directions.

3.4 Deformation mechanism of SnSe under shear loads

The atomic positions and the typical bond lengths and the bond angles under different shear loads are extracted to reveal the shear deformation mechanism of SnSe. Figure 3 shows the deformations of SnSe at critical strains for shearing along the (100)/<001> slip system. At 0.081 strain corresponding to the ideal strength, the structure uniformly resist the shear deformation, as shown in Figure 3(a). With the strain increasing to 0.221, the Se-Sn layered substructure doesn't change significantly, but a relative slip can be observed between the different Se-Sn layered substructures as displayed in Figure 3(b), which can be attributed to the weak van der Waals-like Sn−Se bonding between layered substructures. This slip, releasing the shear stress, accounts for the decreased structural strength as shown in Figure 2. At fracture strain of 0.231, the further relative slip of the layered substructures leads to the shear stress releasing to zero, representing the structure can no longer resist the external deformation, hence resulting in the failure of SnSe.

To further understand the deformation mechanism for shearing along the (100)/<001> slip system, the typical bond lengths (Se1−Sn1, Se1−Sn2, Se1−Sn3) and the bond angle (Se3−Se2−Se4) are shown in figure 3(d). The Se1−Sn1 and Se1−Sn2 covalent bonds are slightly deformed under shear loads with the bond lengths changing from 2.82 and 2.77 Å to 2.85 and 2.75 Å, respectively. Such tiny deformations of these bonds confirm the Se-Sn substructure nearly remains unchanged during the shear process. For the weak van der Waals-like Se1−Sn3 bond, the length initially shrinks with increasing strain, indicating the Se1−Sn3 bond resists shear deformation. At 0.081 strain, the Se−Sn3 bond goes to its minimum length and maximum shear stress of 3.49 Å and 0.59 GPa respectively, representing the bond's maximum resistance. Further increasing shear strain, the Se1−Sn3 bond rapidly stretches, indicating a remarkably reduced bond stiffness. At the material's fracture strain of 0.231, the Se1−Sn3 length increases to 3.73 Å, suggesting the breakage of this softened bond. Moreover, the linear reduction of the Se3−Se2−Se4 bond angle until the strain of 0.081, as shown in Figure 3(d), confirms that the structure uniformly resists shear deformation. At the strain of 0.092, the sudden drop of the bond angle represents the initial slippage of layered Se-Sn substructures. After the drop, the bond angle continues to reduce linearly representing the continuous slippage between the layers, which well explains the releasing shear stress shown in Figure 2. At the fracture strain of 0.231, the bond angle reduces to 51.56° with the shear stress releasing to zero, representing structural failure.

It is noted that the Se1−Sn3 bond first shrinks, then stretches after a critical shear strain of 0.081. This can be explained through the structural deformation. Figure S1 in the supporting information shows the Sn3−Se1−Se5 bond angle and the *c* lattice parameter with increasing shear strain along the (100)/<001> slip system. Increasing the *c* lattice parameter would lead to the

stretching of the Se1−Sn3 bond. On the other hand, the relative slip between different Se-Sn substructures leads to the decreasing obtuse angle of Sn3−Se1−Se5, resulting in a shortening of the Se1−Sn3 bond. The increasing of the *c* lattice parameter and the decreasing of the obtuse angle in Sn3−Se1−Se5 co-determine the deformation of the Se1−Sn3 bond. At the initial stage of shear deformation with shear strain increasing to 0.081, this bond shrinks due to the decreasing obtuse angle of Sn3−Se1−Se5. This dominates the deformation of the Se1−Sn3 bond, which leads to the shrinkage of the Se1−Sn3 bond until shear strain of 0.081, as shown in Figure 3(d). With shear strain further increasing to 0.092 as shown in Figure S1(b) , the *c* lattice parameter rapidly increases and the Sn3−Se1−Se5 bond angle suddenly reduces indicating that the bond stretching due to the increasing *c* lattice parameter dominates the deformation of the Se1−Sn3 bond. This leads to the stretching of the Se1−Sn3 bond after shear strain 0.091, as shown in Figure 3(d).

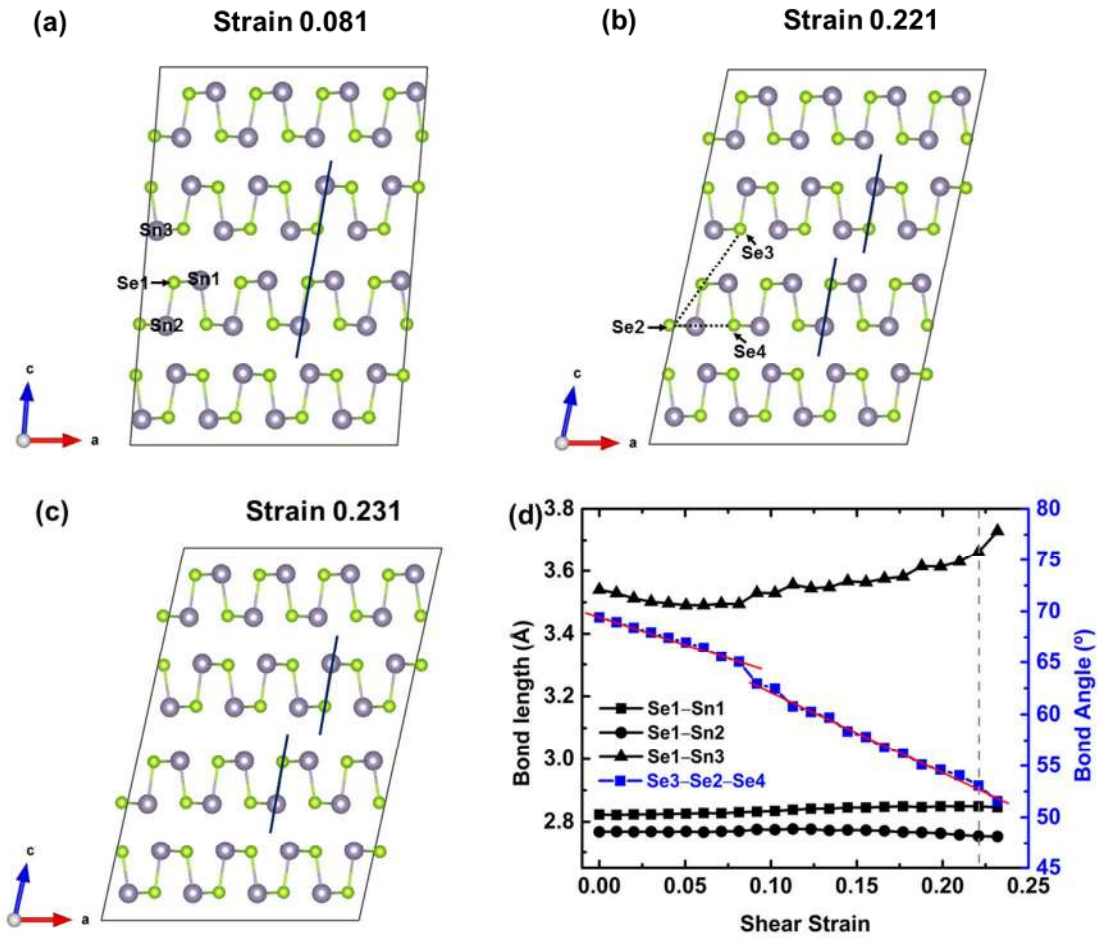

Figure 3. The calculated atomic positions for shear loads along the (100)/<001> slip system: (a) strain 0.081 corresponds to the ideal strength, (b) strain 0.221 before failure strain, (c) fracture strain 0.231. (d)

The average bond lengths (Se1−Sn1, Se1−Sn2, Se1−Sn3) and the bond angle (Se3−Se2−Se4) with the increasing shear strain along the (100)/<001> slip system. The deep green lines plotted in Figure 3(a)-(c) show the slippage of layered Se-Sn substructures. The gray dashed line in Figure 3(d) represents the strain just before failure. The Sn and Se atoms are represented with gray and green balls, respectively.

Figure 4 shows the structural changes in SnSe at various shear strains along the (100)/<010> slip system. The structure is uniformly deformed until the shear strain of 0.102 corresponding to the maximum shear stress. As the shear strain increases to 0.188 before the structural failure, an obvious slippage between layered Se-Sn substructures is shown in Figure 4(b) as similarly observed in Figure 3(b), representing the softened structural rigidity. With the shear strain further increasing to 0.199, the further slippage releases the shear stress to zero, leading to the structural failure. The typical bond lengths of Se−Sn1, Se−Sn2, Se−Sn3 bonds and the bond angle of Sn4−Sn5−Sn6 are plotted against shear strain in Figure 4(d). As the shear strain increases to 0.188 before failure, the Se−Sn1 bond length only changes from 2.81 to 2.85 Å, and the Se−Sn2 bond also change slowly in length from 2.78 to 2.74 Å. This shows that the Se-Sn substructure doesn't weaken much. The Se−Sn3 bond length changes from 3.54 to 3.74 Å with an increase of 5.64%. The large stretching ratio of the Se−Sn3 bond and the almost unchanged Se−Sn1 and Se−Sn2 bonds suggests only the Se−Sn3 bond softens under shear loads, which leads to the monotonously reduced Sn4−Sn5−Sn6 bond angle before failure shown in Figure 4(d) and the slip observed in Figure 4(b). At fracture stain of 0.199, the Se−Sn3 length and the Sn4−Sn5−Sn6 bond angle sharply increases to 4.01 Å and reduces to 68.9° respectively, indicating the breaking of the Se−Sn3 bond and further slip of layered substructures. This leads to the releasing shear stress and the failure of SnSe.

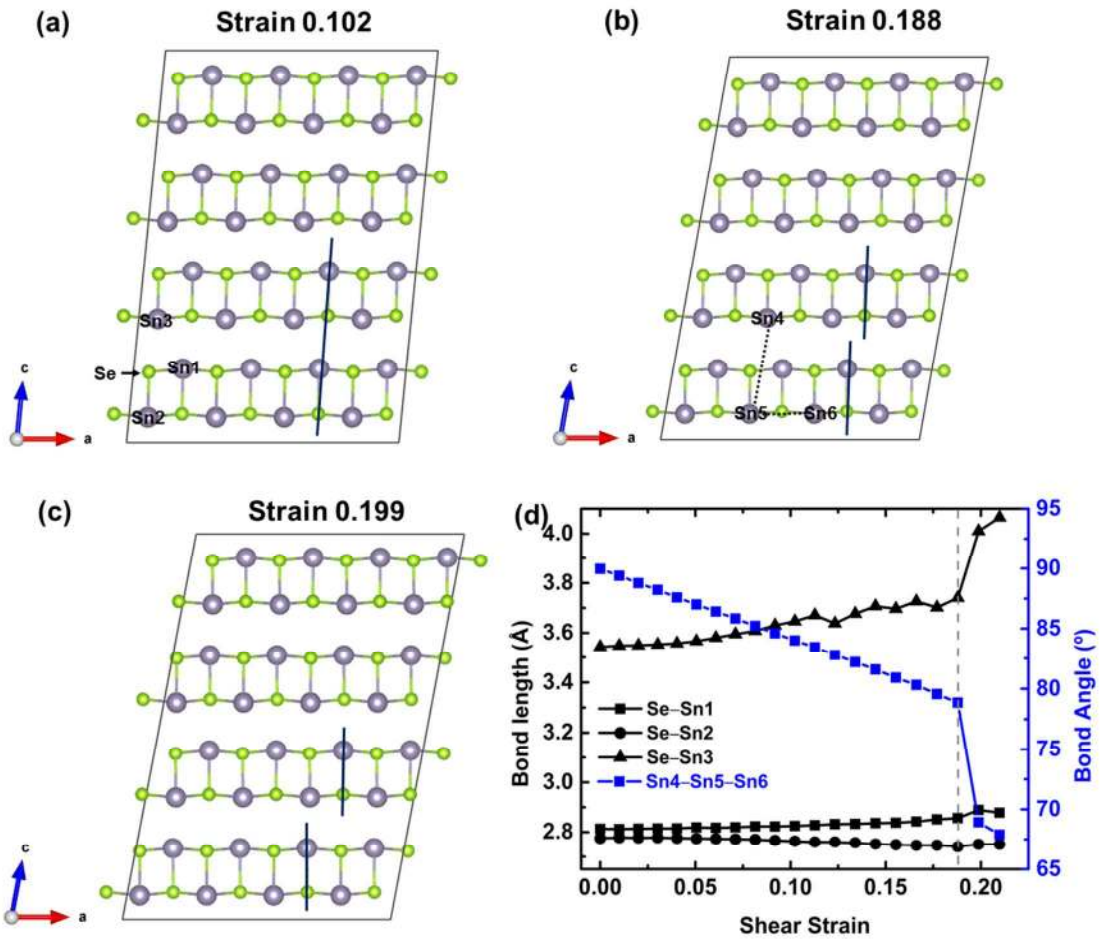

Figure 4. The calculated atomic positions for shear loads along the (100)/<010> slip system: (a) strain 0.102 corresponds to the ideal strength, (b) strain 0.188 before failure strain, (c) fracture strain 0.199. (d) The average bond lengths (Se–Sn1, Se–Sn2, Se–Sn3) and the bond angle (Sn4–Sn5–Sn6) with the increasing shear strain along the (100)/<010> slip system. The deep green lines plotted in Figure 4(a)-(c) show the relative slippage of layered Se-Sn substructures. The gray dashed line in Figure 4(d) represents the strain just before failure.

The selected single layered atomic configurations and typical bond lengths along the (001)/<010> slip system are shown in Figure 5. At the strain of 0.061, Figure 5(a) displays the uniformly deformed structure, resulting in the linearly increased shear stress plotted in Figure 2. At the strain of 0.071, the Se1−Sn1 bond breaks, leading to a sudden decrease in structural rigidity and shear stress. However, the structure can still resist the shear deformation because the newly generated Se1−Sn4 bond holds the structure together. As the strain increases to 0.232, the structure reaches its maximum resistance, leading to its maximum shear stress. With further

increasing strain, the structural rigidity starts to soften, leading to a reduction in shear stress, which corresponds to the 'yielding' stage. At the strain of 0.393 before failure, the structure reaches its resistance limit. At the fracture train of 0.405, the Se1−Sn3 and Se2−Sn1 bonds collapse and the structure releases the shear stress, leading to the structural failure of SnSe. The typical bond lengths of Se1−Sn1, Se1−Sn2, Se1−Sn3, Se1−Sn4, Se2−Sn1 bonds at various shear strains are plotted in Figure 5(d). All the bond lengths continuously change until the strain of 0.061. At the strain of 0.071, the Se1−Sn1 and Se1−Sn4 lengths dramatic changes indicating a significant structure rearrangement displayed in Figure 5(b). Specifically, the Se1−Sn1 length rapidly increases to 3.29 Å, representing the breakage of this bond. Meanwhile, the Se1−Sn4 length sharply decreases to 2.82 Å, representing a bond forming between Se1 and Sn4 atoms. Then, with increasing shear strain, all the bond lengths gradually change until strain 0.393 when the material fails. At the fracture strain of 0.405, the Se1−Sn3 and Se2−Sn1 lengths sharply increase to 3.30 and 3.70 Å, respectively, Such long atomic distances represents the breaking of these two bonds, which deconstructs the structure and leads to the failure of SnSe.

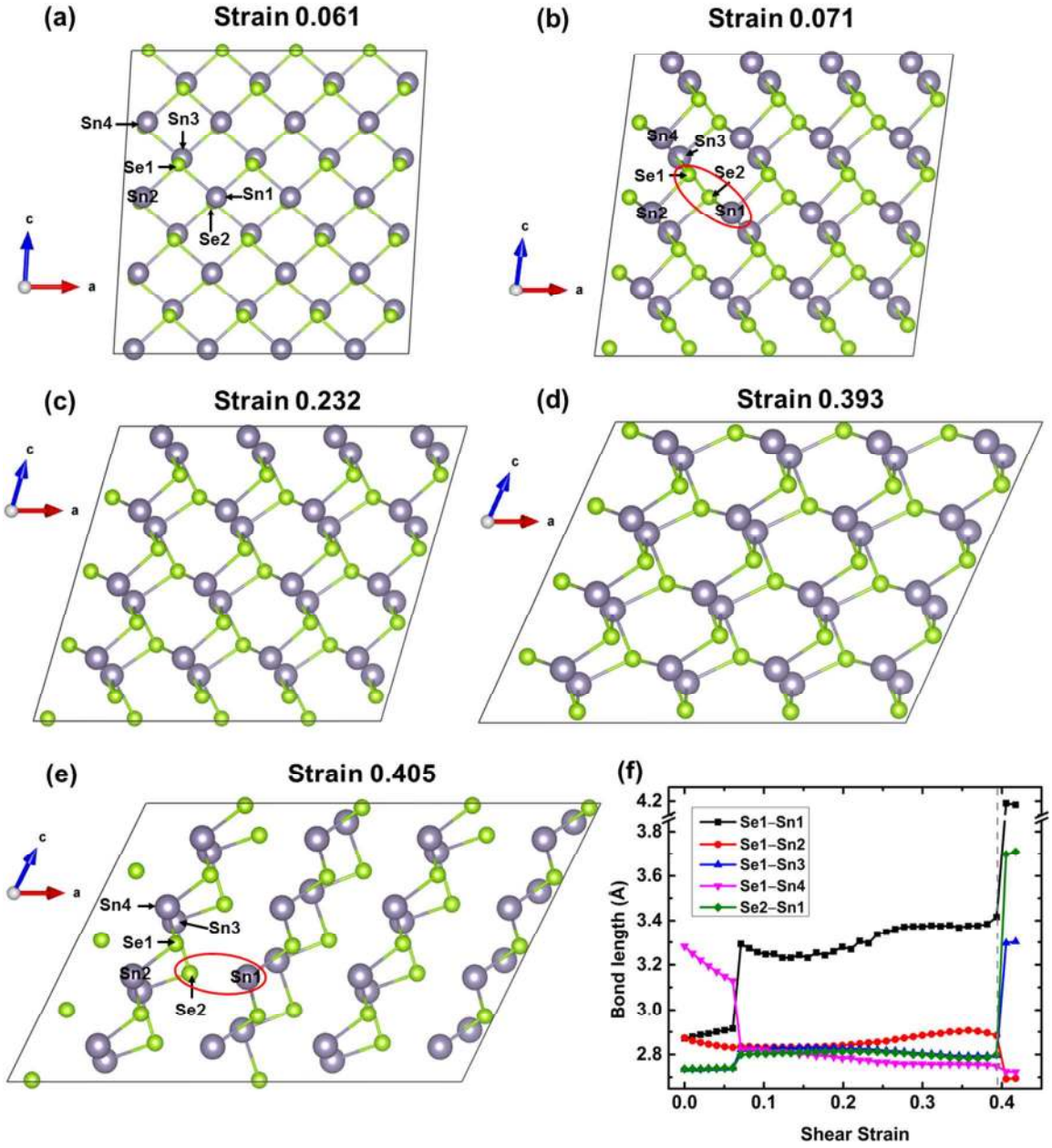

Figure 5. The single layered atomic configurations for shear loads along the (001)/<010> slip system: (a) strain 0.061 corresponds to the ideal strength, (b) strain 0.071 before failure strain, (c) strain 0.0232 corresponds to the ideal strength, (d) strain 0.393 before failure strain, (e) fracture strain 0.405. (f) The average bond lengths (Se1−Sn1, Se1−Sn2, Se1−Sn3, Se1−Sn4, Se2−Sn1) with the increasing shear strain along the (001)/<010> slip system. The red circles plotted in Figure 5(b) and 5(e) show the breakage of Se−Sn bond. The gray dashed line in Figure 5(d) represents the strain just before failure.

3.4 The structural effect on the ideal strength of SnSe

Ideal strength plays an essential role in assessing the reliability of brittle materials.[36,37] The ideal strength reflects the structural maximum resistance on external deformation. In SnSe crystals, the covalent Se–Sn bonds construct the Se-Sn layered substructures, and these layered substructures are coupled by van der Waals-like Se–Sn interactions. Here, we calculate the bonding stiffness in SnSe to understand the structural effect on its ideal strength. Table 2 lists the equilibrium bond length and stretching force constant of the Se–Sn bonding in SnSe. It clearly shows that the Se–Sn bond stiffness gradually weakens with the increasing bond length. The stretching force constant of the van der Waals-like Se–Sn bond is only 0.22 eV/ Å^2, which is much lower than those of the covalent Se–Sn bonds (3.18 and 2.43 eV/ Å^2). This indicates that the van der Waals-like Se–Sn bond is much weaker than the covalent Se–Sn bond in resisting shear deformation, well explaining why the (100)/<001> and (100)/<010> slip systems have a much lower ideal strength compared with the (001)/<010> slip system and why the slip occurs easily between different layered substructures while the layered substructure itself can stably hold together. This agrees well with the experimental observation that SnSe crystals are cleaved along the plane perpendicular to the (100) axis.[20] Experimentally, SnSe crystals suffer from cracks formed during the crystal growth and preparation process,[13] which might affect the thermal conductivity measurements and partially account for the (controversial) ultralow thermal conductivity observed in some SnSe crystals.[23]

Table 2. Calculated equilibrium bond length and stretching force constant in SnSe crystals. The calculation was implemented with the ATAT code.[42]

Bond	Short covalent Se–Sn	Long covalent Se–Sn	van der Waals-like Se–Sn
Equilibrium length (Å)	2.78	2.83	3.44
Stretching force constant (eV/Å^2)	3.18	2.43	0.22

To enhance the ideal strength of SnSe, we suggest improving the van der Waals-like Se–Sn coupling interactions between layered substructures to prevent or postpone slip by introducing the extrinsic dopants into the structure. For example, the partial substitution of Sn by Ge or Se by S could be an effective way to strengthen the van der Waals-like Se–Sn coupling interactions because of the higher stretching force constants of Se–Ge or S–Sn bonds compared with the Se–Sn bond.[43]

4. CONCLUSIONS

We used density functional theory to study the intrinsic mechanical behavior of SnSe under various shear loads focusing on the deformation mechanism. We find that shearing along the (100)/<001> slip system has the lowest ideal strength of 0.59 GPa, which can be attributed to the weak van der Waals-like Se−Sn bond. The failure in this slip system mainly arises from the Se-Sn layered substructures sliding past one another. The (001)/<010> slip system has a higher ideal strength of 2.81 GPa compared with (100)/<001> and (100)/<010> slip systems because the covalent Se−Sn bond is much stronger than the van der Waals-like Se−Sn bond in resisting shear deformation.. To enhance the ideal strength, we suggest improving the van der Waals-like Se−Sn coupling interactions between layered substructures by proper doping strategies, *e.g.,* the partial substitution of Sn by Ge or Se by S.

ACKNOWLEDGEMENTS

This work is partially supported by National Basic Research Program of China (973-program) under Project No. 2013CB632505, the 111 Project of China under Project No. B07040, Materials Project by Department of Energy Basic Energy Sciences Program under Grant No. EDCBEE, DOE Contract DE-AC02-05CH11231, and China Postdoctoral Science Foundation (408-32200031). We would like to acknowledge the Jet Propulsion Laboratory, California Institute of Technology, as a funding source under a contract with the National Aeronautics and Space Administration, which was supported by the NASA Science Missions Directorate's Radioisotope Power Systems Technology Advancement Program.

Supporting information. The Sn3−Se1−Se5 bond angle and the *c*-axis lattice parameter with the increasing shear strain along the (100)/<001> slip system.

REFERENCES

(1) Bell, L. E., Cooling, Heating, Generating Power, and Recovering Waste Heat with Thermoelectric Systems. *Science.* **2008**, *321*, 1457-1461.

(2) Snyder, G. J.; Toberer, E. S. Complex Thermoelectric Materials. *Nat. Mater.* **2008**, 7, 105-114.

(3) Snyder, G. J.; Christensen, M.; Nishibori, E.; Caillat, T.; Iversen, B. B., Disordered Zinc in Zn_4Sb_3 with Phonon-Glass and Electron-Crystal Thermoelectric Properties. *Nat Mater.* **2004**, 3, 458-463.

(4) Nolas, G. S.; Morelli, D. T.; Tritt, T. M. Skutterudites: A Phonon-Glass-Electron Crystal Approach to Advanced Thermoelectric Energy Conversion Applications. *Annu. Rev. Mater. Sci.* **1999**, 29, 89-116.

(5) Pei, Y.; Shi, X.; LaLonde, A.; Wang, H.; Chen, L.; Snyder, G. J., Convergence of Electronic Bands for High Performance Bulk Thermoelectrics. *Nature.* **2011,** 473, 66-69.

(6) Tang, Y. L.; Gibbs, Z. M.; Agapito, L. A.; Li, G.; Kim, H. S.; Nardelli, M. B.; Curtarolo, S.; Snyder, G. J., Convergence of Multi-Valley Bands as the Electronic Origin of High Thermoelectric Performance in $CoSb_3$ Skutterudites. *Nat Mater.* **2015**, 14, 1223-1228.

(7) Lan, Y. C.; Minnich, A. J.; Chen, G.; Ren, Z. F., Enhancement of Thermoelectric Figure-of-Merit by a Bulk Nanostructuring Approach. *Adv. Func. Mater.* **2010**, 20, 357-376.

(8) Hsu, K. F.; Loo, S.; Guo, F.; Chen, W.; Dyck, J. S.; Uher, C.; Hogan, T.; Polychroniadis, E. K.; Kanatzidis, M. G., Cubic $AgPb_mSbTe_{2+m}$: Bulk Thermoelectric Materials with High Figure of Merit. *Science.* **2004**, 303, 818-821.

(9) Dresselhaus, M. S.; Chen, G.; Tang, M. Y.; Yang, R. G.; Lee, H.; Wang, D. Z.; Ren, Z. F.; Fleurial, J. P.; Gogna, P., New Directions for Low-Dimensional Thermoelectric Materials. *Adv. Mater.* **2007**, 19, 1043-1053.

(10) Morelli, D. T.; Jovovic, V.; Heremans, J. P., Intrinsically Minimal Thermal Conductivity in Cubic I-V-VI(2) Semiconductors. *Phys. Rev. Lett.* **2008**, 101, 035901.

(11) Nielsen, M. D.; Ozolins, V.; Heremans, J. P., Lone Pair Electrons Minimize Lattice Thermal Conductivity. *Energ. Environ. Sci.* **2013**, 6, 570-578.

(12) Barako, M. T.; Park, W.; Marconnet, A. M.; Asheghi, M.; Goodson, K. E., Thermal Cycling, Mechanical Degradation, and the Effective Figure of Merit of a Thermoelectric Module. *J. Electron. Mater.* **2013**, *42*, 372-381.

(13) Zhao, L. D.; Lo, S. H.; Zhang, Y.; Sun, H.; Tan, G.; Uher, C.; Wolverton, C.; Dravid, V. P.; Kanatzidis, M. G., Ultralow Thermal Conductivity and High Thermoelectric Figure of Merit in SnSe Crystals. *Nature.* **2014,** 508, 373-377.

(14) Zhang, Q.; Chere, E. K.; Sun, J. Y.; Cao, F.; Dahal, K.; Chen, S.; Chen, G.; Ren, Z. F., Studies on Thermoelectric Properties of n-type Polycrystalline $SnSe_{1-x}S_x$ by Iodine Doping. *Adv. Energy. Mater.* **2015**, 5, 1500360.

(15) Carrete, J.; Mingo, N.; Curtarolo, S., Low Thermal Conductivity and Triaxial Phononic Anisotropy of SnSe. *Appl. Phys. Lett.* **2014**, 105, 101907.

(16) Chen, C. L.; Wang, H.; Chen, Y. Y.; Day, T.; Snyder, G. J., Thermoelectric Properties of p-type Polycrystalline SnSe Doped with Ag. *J. Mater. Chem. A.* **2014**, 2, 11171-11176.

(17) Wei, T. R.; Tan, G. J.; Zhang, X. M.; Wu, C. F.; Li, J. F.; Dravid, V. P.; Snyder, G. J.; Kanatzidis, M. G., Distinct Impact of Alkali-Ion Doping on Electrical Transport Properties of Thermoelectric p-Type Polycrystalline SnSe. *J. Am. Chem. Soc.* **2016**, 138, 8875-8882.

(18) Ding, G. Q.; Gao, G. Y.; Yao, K. L., High-Efficient Thermoelectric Materials: The Case of Orthorhombic IV-VI Compounds. *Sci. Rep-Uk.* **2015**, 5, 9567.

(19) Agarwal, A.; Vashi, M. N.; Lakshminarayana, D.; Batra, N. M., Electrical Resistivity Anisotropy in Layered p-SnSe Single Crystals. *J. Mater. Sci-Mater. El.* **2000**, 11, 67-71.

(20) Zhao, L. D.; Tan, G. J.; Hao, S. Q.; He, J. Q.; Pei, Y. L.; Chi, H.; Wang, H.; Gong, S. K.; Xu, H. B.; Dravid, V. P.; Uher, C.; Snyder, G. J.; Wolverton, C.; Kanatzidis, M. G., Ultrahigh Power Factor and Thermoelectric Performance in Hole-Doped Single-Crystal SnSe. *Science.* **2016**, 351, 141-144.

(21) Biswas, K.; He, J. Q.; Blum, I. D.; Wu, C. I.; Hogan, T. P.; Seidman, D. N.; Dravid, V. P.; Kanatzidis, M. G., High-Performance Bulk Thermoelectrics with All-Scale Hierarchical Architectures. *Nature.* **2012**, 489, 414-418.

(22) Bae, K. H.; Choi, S. M.; Kim, K. H.; Choi, H. S.; Seo, W. S.; Kim, I. H.; Lee, S.; Hwang, H. J. Power-Generation Characteristics After Vibration and Thermal Stresses of Thermoelectric Unicouples with $CoSb_3$ /Ti/Mo(Cu) Interfaces. *J. Electron. Mater.* **2015**, 44, 2124-2131.

(23) Wei, P. C.; Bhattacharya, S.; He, J.; Neeleshwar, S.; Podila, R.; Chen, Y. Y.; Rao. A. M., The Intrinsic Thermal Conductivity of SnSe. *Nature.* **2016**, 539, E1-E2.

(24) Ibrahim, D.; Vaney, J. B.; Sassi, S.; Candolfi, C.; Ohorodniichuk, V.; Levinsky, P.; Semprimoschnig, C.; Dauscher, A.; Lenoir, B., Reinvestigation of the Thermal Properties of Single-Crystalline SnSe. *Appl. Phys. Lett.* **2017,** *110*, 032103.

(25) Zhang, Q.; Chere, E. K.; Sun, J.; Cao, F.; Dahal, Keshab.; Chen, Shuo.; Chen, G.; Ren, Z., Studies on Thermoelectric Properties of n-type Polycrystalline $SnSe_{1-x}S_x$ by Iodine Doping. *Adv. Energy Mater.* **2015**, 5, 1500360

(26) Chere, E. K.; Zhang, Q.; Dahal, K.; Cao, F.; Mao, J.; Ren, Z., Studies on Thermoelectric Figure of Merit of Na-Doped p-Type Polycrystalline SnSe. *J. Mater. Chem. A.* **2016,** *4*, 1848-1854.

(27) Chen, C.-L.; Wang, H.; Chen, Y.-Y.; Day, T.; Snyder, G. J., Thermoelectric Properties of p-Type Polycrystalline SnSe Doped with Ag. *J. Mater. Chem. A.* **2014**, 2, 11171-11176.

(28) Sassi, S.; Candolfi, C.; Vaney, J. B.; Ohorodniichuk, V.; Masschelein, P.; Dauscher, A.; Lenoir, B., Assessment of the Thermoelectric Performance of Polycrystalline p-Type SnSe. *Appl. Phys. Lett.* **2014**, 104, 212105.

(29) Wang, X.; Xu, J.; Liu, G.; Fu, Y.; Liu, Z.; Tan, X.; Shao, H.; Jiang, H.; Tan, T.; Jiang, J., Optimization of Thermoelectric Properties in n-Type SnSe Doped with $BiCl_3$. *Appl. Phys. Lett.* **2016**, 108, 083902.

(30) Kresse, G.; Furthmuller, J. Efficiency of ab-initio Total Energy Calculations for Metals and Semiconductors Using a Plane-Wave Basis Set. *Comp. Mater. Sci.* **1996**, 6, 15-50.

(31) Kresse, G.; Furthmuller, J. Efficient Iterative Schemes for ab initio Total-Energy Calculations Using a Plane-Wave Basis Set. *Phys. Rev. B.* **1996**, 54, 11169-11186.

(32) Kresse, G.; Joubert, D. From Ultrasoft Pseudopotentials to the Projector Augmented-Wave Method. *Phys. Rev. B.* **1999**, 59, 1758-1775.

(33) Wiedemeier, H.; Schnering, H. G. V., Refinement of the Structures of GeS, GeSe, SnS and SnSe. *Z Kristallogr.* **1978**, 148, 295-303.

(34) Jain, A.; Ong, S. P.; Hautier, G.; Chen, W.; Richards, W. D.; Dacek, S.; Cholia, S.; Gunter, D.; Skinner, D.; Ceder, G.; Persson, K. A., Commentary: The Materials Project: A Materials Genome Approach to Accelerating Materials Innovation. *Apl. Mater.* **2013,** 1, 011002.

(35) Li, G. D.; An, Q.; Li, W. J.; Goddard, W. A.; Zhai, P. C.; Zhang, Q. J.; Snyder, G. J., Brittle Failure Mechanism in Thermoelectric Skutterudite $CoSb_3$. *Chem. Mater.* **2015**, 27, 6329-6336.

(36) Ogata, S.; Li, J.; Yip, S. Ideal Pure Shear Strength of Aluminum and Copper. *Science.* **2002**, 298, 807-811.

(37) Roundy, D.; Krenn, C. R.; Cohen, M. L.; Morris, J. W. Ideal Shear Strengths of fcc Aluminum and Copper. *Phys. Rev. Lett.* **1999**, 82, 2713-2716.

(38) Chung, D. H. Elastic Moduli of Single-Crystal and Polycrystalline MgO. *Philos. Mag.* **1963**, 8, 833-841.

(39) de Jong, M.; Chen, W.; Angsten, T.; Jain, A.; Notestine, R.; Gamst, A.; Sluiter, M.; Krishna Ande, C.; van der Zwaag, S.; Plata, J. J.; Toher, C.; Curtarolo, S.; Ceder, G.; Persson, K. A.; Asta, M., Charting the Complete Elastic Properties of Inorganic Crystalline Compounds. *Sci. data.* **2015**, 2, 150009.

(40) Pugh, S. F., Relations between the Elastic Moduli and the Plastic Properties of Polycrystalline Pure Metals. *Philos. Mag.* **1954**, *45*, 823-843.

(41) Li, G. D.; An, Q.; Aydemir, U.; Goddard, W. A., III; Wood, M.; Zhai, P. C.; Zhang, Q. J.; Snyder, G. J., Enhanced Ideal Strength in the Thermoelectric Half-Heusler TiNiSn by Sub-Structure Engineering. *J. Mater. Chem. A.* **2016**, 4, 14625-14636.

(42) Walle, A.; Asta, M.; Ceder, G., The Alloy Theoretic Automated Toolkit: A User Guide. *Calphad.* **2002**, *26*, 539-553.

(43) Murase, K.; Fukunaga, T.; Yakushiji, K.; Yoshimi, T.; Yunoki, I., Investigation of Stability of (Ge,Sn)-(S, or Se)42 Cluster by Vibrational-Spectra. *J. Non-Cryst. Solids.* **1983**, 59-60, 883-886.

TOC Graphic:

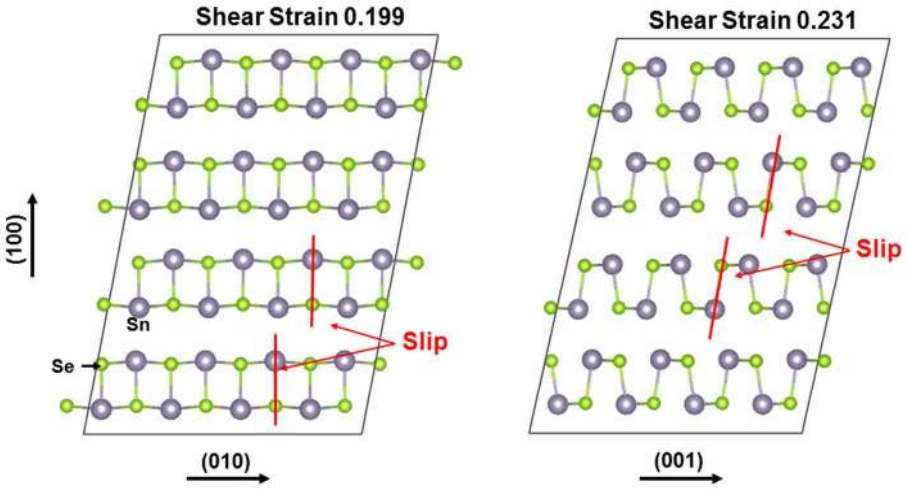
Shear Strain 0.199
Shear Strain 0.231
(100)
Sn
Se
Slip
Slip
(010)
(001)